

Temperature Coefficient of Frequency Modeling for CMOS-MEMS Bulk Mode Composite Resonators

Siping Wang, *Student Member, IEEE*, Wen-Chien Chen, *Member, IEEE*,
 Bichoy Bahr, *Student Member, IEEE*, Weileun Fang, *Member, IEEE*,
 Sheng-Shian Li, *Member, IEEE*, and Dana Weinstein, *Member, IEEE*

Abstract—CMOS-MEMS resonators, which are promising building blocks for achieving monolithic integration of MEMS structure, can be used for timing and filtering applications, and control circuitry. SiO_2 has been used to make MEMS resonators with quality factor $Q > 10^4$, but temperature instability remains a major challenge. In this paper, a design that uses an embedded metal block for temperature compensation is proposed and shows sub-ppm temperature stability (-0.21 ppm/K). A comprehensive analytical model is derived and applied to analyze and optimize the temperature coefficient of frequency (TCF) of the CMOS-MEMS composite material resonator. Comparison with finite element method simulation demonstrates good accuracy. The model can also be applied to predict and analyze the TCF of MEMS resonators with arbitrary mode shape, and its integration with simulation packages enables interactive and efficient design process.

I. INTRODUCTION

VIBRATING micromechanical resonators capable of providing high Q and zero dc power consumption have been implemented for timing references in a variety consumer electronics [1] [2]–[4], leading to smaller size and lower cost compared with conventional electrical components, such as crystal [5], [6], SAW [7], and film bulk acoustic resonator (FBAR) [8] resonators. Nevertheless, the discrete nature of these off-chip micromechanical resonators still impedes the system miniaturization and circuit integration for future multiband, multimode wireless transceivers [9], vibrational inertial sensors [10], and timing references [11], [12]. To realize MEMS resonators monolithically integrated with circuitry, in recent years CMOS-MEMS resonator platforms based on a foundry-oriented $0.35 \mu\text{m}$ 2-poly-4-metal (2P4M) CMOS technology [13]–[15] and $0.18 \mu\text{m}$ 1-poly-6-metal (1P6M) CMOS process [16], [17] have been developed to fabricate integrated vibrating micromechanical structures side by side

with circuits. However, due to the limited structural material option (i.e., metal and oxide) in CMOS technology, CMOS-MEMS resonators are mostly made of metal-rich structures, suffering relatively low Q and poor thermal stability [15], as compared with conventional silicon-based resonators. To solve the low- Q issues resulting from metal, a square plate oxide resonator composed of silicon dioxide (SiO_2) with embedded metal electrodes via a CMOS $0.18 \mu\text{m}$ process and a metal etching technique has been successfully developed with resonator Q exceeding 10000 [18], as shown in Fig. 1. But this design has poor thermal stability due to the oxide-rich structure, which has a positive temperature coefficient of Young's modulus (+TCE) [19].

To address thermal stability of capacitively transduced resonators, researchers have demonstrated passive temperature compensation techniques, such as the stress induced frequency compensation [20], composite structures consisting of silicon dioxide [21]–[23], and degenerate doping [24]–[26], without consuming excessive power [27] or requiring complicated active compensation parabolic-type control circuits [28], [29]. Among these passive approaches, composite structures consisting of silicon dioxide have recently become mainstream to achieve first-stage temperature compensation; because it is easy to process and has TCE of opposite sign relative to most other materials commonly used in CMOS-MEMS, it can thus be used to negate the temperature dependence of other materials. However, the temperature coefficient of frequency (TCF) for complicated composite structures can be difficult to control and predict analytically, leading to time-consuming simulations and a nonintuitive design process. In this work, we propose an analytical model for TCF based on perturbation theory capable of analyzing composite and unreleased structures with arbitrary material distribution and suitable for arbitrary composite material resonators. The model greatly accelerates the simulation process involved in designing a thermally stable resonant structure. As will be shown, the first-order TCF can be lowered from high positive value (+93 ppm/K) without compensation to sub-ppm level (-0.28 ppm/K) with the proposed compensation (according to simulation). The latter meets the requirement of high performance micromechanical oscillator for future timing devices or frequency synthesizer applications.

Manuscript received October 10, 2014; accepted March 14, 2015.

S. Wang and W.-C. Chen contributed equally to this work.

S. Wang, B. Bahr, and D. Weinstein are with the Department of Electrical Engineering and Computer Science, Massachusetts Institute of Technology, Cambridge, MA 02139, USA (e-mail: spinwang@mit.edu).

W.-C. Chen, W. Fang, and S.-S. Li are with National Tsing Hua University, Hsinchu, Taiwan.

From mid-2012 to mid-2013, W.-C. Chen was with Prof. Dana Weinstein at the Massachusetts Institute of Technology, Cambridge, as a Visiting Student.

DOI <http://dx.doi.org/10.1109/TUFFC.2014.006724>

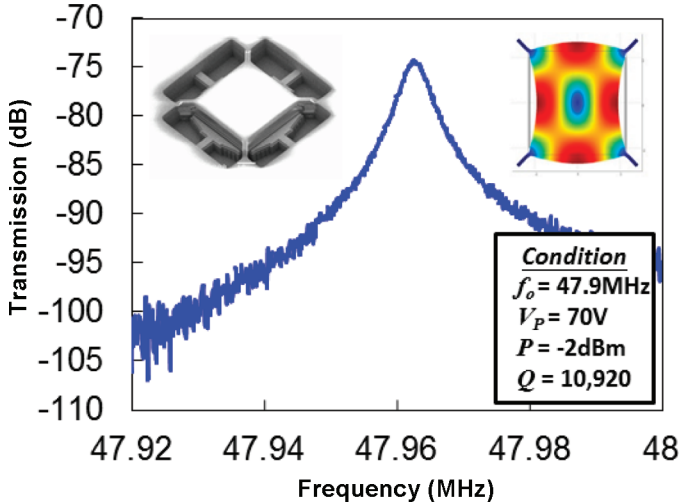


Fig. 1. A CMOS-MEMS Lamé mode resonator composed of SiO_2 , demonstrating $Q > 10^4$.

II. MODELING OF TEMPERATURE COEFFICIENT OF FREQUENCY

To demonstrate the ability to tune the thermal stability of bulk mode resonators, an oxide (+TCE) structure is embedded with metal (-TCE) blocks using CMOS-MEMS technology, achieving passive temperature compensation. This leads to the possibility of achieving a CMOS-MEMS resonator with high- Q as well as low TCF. A 0.18- μm 1-poly-6-metal standard CMOS process with diverse structural configuration and flexible material option is utilized to construct the composite bulk acoustic Lamé mode resonator. The resonator can be modeled as the parallel combination of multiple square plates made of different material compositions as shown in Fig. 2, and each of these plates can be treated as a separate Lamé mode resonator. The thickness of mat.1 ($h_{\text{mat.1}}$) and mat.2 ($h_{\text{mat.2}}$) is 0.53 and 0.85 μm , respectively, and the plate side length is 22.95 μm . Driving and sensing capacitors have a gap size of 0.42 μm . Anchors are drawn to scale in Fig. 2. Because layer thickness h is small compared with resonator side length, plane stress approximation is used and vibration is assumed to be 2-D only, with no dependence on the thickness dimension. The structure is composed of 3 types of plates: a metal-based plate embedded with oxide blocks (mat.1), an oxide-based plate embedded with metal blocks (mat.2), and one made purely of oxide (oxide). The embedded metal electrodes and oxide edge for etching protection [18] are neglected for a simplified illustration of the model, but will be included in the reported TCF of the final design. The overall linear TCF of the composite body is given as a linear combination of the TCFs of each single layer plate, as shown in (1). Detailed derivation is provided in Appendix A.

$$\text{TCF} = \frac{A \cdot \text{TCF}_{\text{mat.1}} + B \cdot \text{TCF}_{\text{mat.2}} + C \cdot \text{TCF}_{\text{ox}}}{A + B + C}, \quad (1)$$

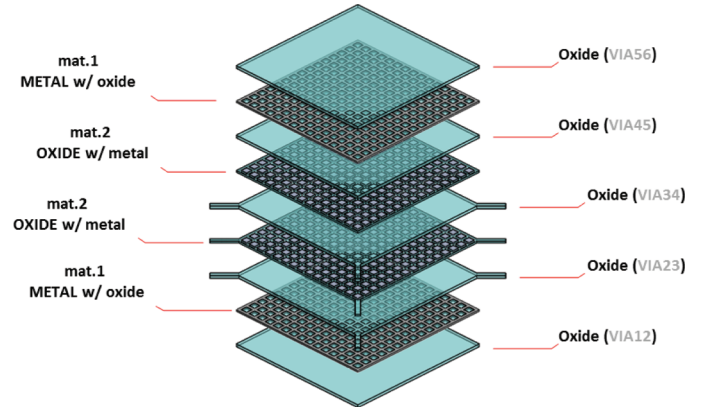


Fig. 2. Composite material multilayer Lamé mode CMOS-MEMS resonator for temperature compensation. The structure can be viewed as the parallel combination of 9 single layer plates. Two layers of mat.1, 2 layers of mat.2, and 5 layers of oxide.

where

$$A = h_{\text{mat.1}} \rho_{\text{mat.1}} f_{\text{mat.1}}^2, \quad (2)$$

$$B = h_{\text{mat.2}} \rho_{\text{mat.2}} f_{\text{mat.2}}^2, \quad (3)$$

$$C = h_{\text{ox}} \rho_{\text{ox}} f_{\text{ox}}^2. \quad (4)$$

In the above expressions, for a particular plate of type "mat," TCF_{mat} is the TCF calculated for each single layer, h_{mat} is the layer thickness, f_{mat} is the resonant frequency of that single layer plate, and ρ_{mat} is the plate's effective density,

$$\rho_{\text{mat}} = \frac{\int_{\Omega} \rho(x, y) u^2(x, y) d\Omega}{\int_{\Omega} u^2(x, y) d\Omega}, \quad (5)$$

where Ω represents resonator's spatial domain. The thickness of each layer is defined by the foundry, and thus h_{mat} is known from the design. TCF_{mat} and f_{mat} are variables dependent on the design, namely, embedding of compensating material. A fast analytical model for deriving these values given a certain design is the focus of the rest of this paper.

The overall TCF of a multilayer composite resonator can be calculated if the resonant frequency and TCF of each type of single layer plate are known. In this section, an analytical model for predicting the resonant frequencies and TCF of a generalized composite bulk acoustic resonator is presented. This analytical model lays the foundation for calculating and optimizing the TCF of the aforementioned multilayer CMOS-MEMS resonator, but it can also be applied to quickly calculate the TCF of any MEMS resonator given its material composition and mode shape. For this particular multilayer CMOS-MEMS resonator, as will be shown in Section III, all the variables needed to calculate the overall TCF of the multilayer composite material resonator can be derived based on the unperturbed 2-D Lamé mode shape and material properties using this analytical model.

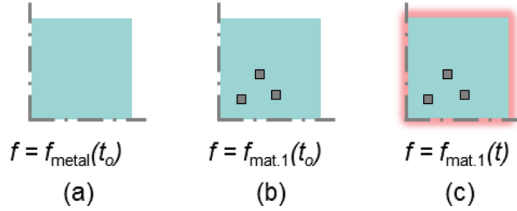


Fig. 3. (a) Homogeneous metal plate. (b) Oxide blocks are embedded. (c) Temperature change then induces further frequency shift.

A. Frequency Perturbation Due to a Change in Material Property

The resonance frequency of a mechanical resonator shifts due changes in material properties and temperature. As will be shown later, temperature change leads directly to change in material properties. As shown in Fig. 3, a metal-based plate is used as an example. At room temperature, the resonant frequency of a purely metal resonator [Fig. 3(a)] is $f_{\text{metal}}(t_0)$. Embedding with oxide blocks shifts the room temperature resonant frequency to $f_{\text{mat.1}}(t_0)$ [Fig. 3(b)]. Temperature will further shift the resonant frequency of this composite material resonator to $f_{\text{mat.1}}(t)$ [Fig. 3(c)]. Perturbation theory is used to understand the above process and provide an analytical model to predict frequency shift due to material change and temperature change. A quarter plate is used here due to the symmetry of the Lamé mode, as shown in the inset of Fig. 1.

The elastic field equations are formulated as a generalized Hermitian eigenproblem, which offers an elegant expression for the resonant frequency shift and an intuitive approach to study the relationship between frequency and material property of all resonant structures. In the absence of external driving force, the acoustic field obeys the following equations [30]:

$$\nabla \cdot T = \frac{\partial \rho v}{\partial \tau}, \quad (6)$$

$$\nabla_s v = \frac{\partial S}{\partial \tau}, \quad (7)$$

where T , ρ , v , τ , and S represent stress field, density, velocity field, time, and strain field, respectively. Eq. (6) is the equation of motion, and (7) is the time derivative of the strain-displacement relation. The stress and strain tensors are simplified to two 6-dimensional vectors, using Voigt notation, which simplifies a full pair of subscripts to a single abbreviated subscript. The two differential operators are divergence operator and strain-displacement operator, respectively. They are defined as follows [30]:

$$\nabla \cdot = \begin{bmatrix} \partial/\partial x & 0 & 0 & 0 & \partial/\partial z & \partial/\partial y \\ 0 & \partial/\partial y & 0 & \partial/\partial z & 0 & \partial/\partial x \\ 0 & 0 & \partial/\partial z & \partial/\partial y & \partial/\partial x & 0 \end{bmatrix}, \quad (8)$$

$$\nabla_s = \begin{bmatrix} \partial/\partial x & 0 & 0 & 0 & \partial/\partial z & \partial/\partial y \\ 0 & \partial/\partial y & 0 & \partial/\partial z & 0 & \partial/\partial x \\ 0 & 0 & \partial/\partial z & \partial/\partial y & \partial/\partial x & 0 \end{bmatrix}^T. \quad (9)$$

Thus, the time harmonic acoustic field equation can be simplified into the following form:

$$-\nabla \cdot c : \nabla_s u = \omega^2 \rho u, \quad (10)$$

where u is the displacement field and c is the stiffness matrix. This is of the form of a generalized Hermitian eigenvalue problem:

$$\hat{\mathbf{A}} u = \lambda \hat{\mathbf{B}} u, \quad (11)$$

where

$$\hat{\mathbf{A}} = -\nabla \cdot c : \nabla_s, \quad (12)$$

$$\hat{\mathbf{B}} = \rho, \quad (13)$$

$$\lambda = \omega^2. \quad (14)$$

In this formulation, $\hat{\mathbf{A}}$ and $\hat{\mathbf{B}}$ are Hermitian operators, and λ is the eigenvalue and equals angular resonance frequency squared.

Before perturbation is introduced into the system, some mathematical notations and identities need to be defined:

1) Double Dot Tensor Product: The double dot tensor product notation used above implies the summation over pairs of repeated full subscript (kl) or summation over repeated single abbreviated subscript (J). For example the stress can be expressed as

$$T : S = \sum_{ij} T_{ij} S_{ij} = \sum_J T_J S_J, \quad (15)$$

$$T = c : S = \sum_{kl} c_{ijkl} S_{kl} = \sum_J c_{IJ} S_J. \quad (16)$$

2) $\langle u_1 | u_2 \rangle$: This denotes the inner product of a two-vector field and is defined as

$$\langle u_1 | u_2 \rangle = \int_{\Omega} u_1^* \cdot u_2 d\Omega. \quad (17)$$

The superscript * indicates complex conjugate. Complex phasor quantities are used to represent strain and stress fields for algebraic simplification.

3) $\langle \nabla_s u | T \rangle = -\langle u | \nabla \cdot T \rangle$: This is a useful equality relationship, which is crucial to the derivation. It states that ∇_s is the adjoint of $-\nabla \cdot$. Detailed proof is provided in Appendix B.

4) $\hat{\mathbf{A}}$ and $\hat{\mathbf{B}}$ Are Both Hermitian: This leads to the fact that $\hat{\mathbf{A}} u = \lambda \hat{\mathbf{B}} u$ is a generalized Hermitian eigenproblem with real eigenvalues and orthogonal eigenfunctions. Detailed proof is provided in Appendix C.

Under the framework of this generalized Hermitian eigenproblem, now perturbation is added to the system. In the case of passive compensation using composite materials, the perturbation is due to a shift in material property as the embedded material is different from the original

material. In this case, aluminum is embedded in SiO_2 and vice versa. Perturbations are added to the operators, eigenfunction and eigenvalue. Superscript indicates the order of the perturbation; 0 represents the original unperturbed system and 1 represents the first-order perturbation. In this analysis, higher order perturbations are ignored.

$$\begin{aligned}\hat{\mathbf{A}} &= \hat{\mathbf{A}}^0 + \hat{\mathbf{A}}^1 + \dots \\ \hat{\mathbf{B}} &= \hat{\mathbf{B}}^0 + \hat{\mathbf{B}}^1 + \dots \\ \hat{\lambda} &= \hat{\lambda}^0 + \hat{\lambda}^1 + \dots \\ \hat{u} &= \hat{u}^0 + \hat{u}^1 + \dots\end{aligned}\quad (18)$$

The original unperturbed field and the new field both obey the generalized Hermitian eigenproblem. Thus

$$\begin{aligned}\hat{A}^0 u^0 &= \lambda^0 \hat{B}^0 u^0 (\hat{A}^0 + \hat{A}^1)(u^0 + u^1) \\ &= (\lambda^0 + \lambda^1)(\hat{B}^0 + \hat{B}^1)(u^0 + u^1).\end{aligned}\quad (19)$$

The zeroth order terms cancel out and the first-order perturbation simplifies to

$$\hat{A}^1 u^0 + \hat{A}^0 u^1 = \lambda^0 \hat{B}^1 u^0 + \lambda^0 \hat{B}^0 u^1 + \lambda^1 \hat{B}^0 u^0. \quad (20)$$

Performing an inner product with the unperturbed field u^0 yields

$$\begin{aligned}\langle u^0 | \hat{A}^1 u^0 \rangle + \langle u^0 | \hat{A}^0 u^1 \rangle &= \\ \langle u^0 | \lambda^0 \hat{B}^1 u^0 \rangle + \langle u^0 | \lambda^0 \hat{B}^0 u^1 \rangle + \langle u^0 | \lambda^1 \hat{B}^0 u^0 \rangle &.\end{aligned}\quad (21)$$

Because \hat{A} and \hat{B} are both Hermitian and the unperturbed field still obeys the original eigenequation, it follows that

$$\langle u^0 | \hat{A}^0 u^1 \rangle = \langle \hat{A}^0 u^0 | u^1 \rangle = \langle \lambda^0 \hat{B}^0 u^0 | u^1 \rangle = \langle u^0 | \lambda^0 \hat{B}^0 u^1 \rangle. \quad (22)$$

Consequently, first-order perturbation of the eigenvalue can be derived:

$$\langle u^0 | \hat{A}^1 u^0 \rangle = \langle u^0 | \lambda^0 \hat{B}^1 u^0 \rangle + \langle u^0 | \lambda^1 \hat{B}^0 u^0 \rangle, \quad (23)$$

$$\lambda^1 = \frac{\langle u^0 | \hat{A}^1 u^0 \rangle - \langle u^0 | \lambda^0 \hat{B}^1 u^0 \rangle}{\langle u^0 | \hat{B}^0 u^0 \rangle}, \quad (24)$$

where

$$\begin{aligned}\hat{A}^1 &= -\nabla \cdot \Delta c : \nabla_s, \\ \hat{B}^1 &= \Delta \rho, \\ \lambda^1 &= 2\omega^0 \Delta \omega.\end{aligned}\quad (25)$$

Consequently, the first-order perturbation of the resonant frequency can be derived:

$$2\omega^0 \Delta \omega = \frac{\int_{\Omega} (u^0)^* [-\nabla \cdot \Delta c : \nabla_s u^0] d\Omega - \int \Delta \rho |\omega^0 u^0|^2 d\Omega}{\int_{\Omega} \rho^0 |u^0|^2 d\Omega},$$

$$\frac{\Delta \omega}{\omega^0} = \frac{\int_{\Omega} (u^0)^* [-\nabla \cdot \Delta c : \nabla_s u^0] d\Omega - \int \Delta \rho |\omega^0 u^0|^2 d\Omega}{2 \int_{\Omega} \rho^0 |\omega^0 u^0|^2 d\Omega}.$$

Because $\langle \nabla_s u | T \rangle = -\langle u | \nabla \cdot T \rangle$, the above expression can be rearranged to the following form:

$$\frac{\Delta \omega}{\omega^0} = \frac{\int_{\Omega} (\nabla_s u^0)^* : \Delta c : (\nabla_s u^0) d\Omega - \int \Delta \rho |\omega^0 u^0|^2 d\Omega}{2 \int_{\Omega} \rho^0 |\omega^0 u^0|^2 d\Omega}. \quad (26)$$

Considering that $\nabla_s u^0 = S^0$, thus the first term in the numerator of the (26) can be interpreted as the first-order perturbation in potential energy or strain energy (ΔU) due to change in material stiffness matrix and the second term in the numerator can be interpreted as the first-order perturbation in kinetic energy (ΔK) due to change in material density. Thus the first-order correction of the resonant frequency can be written in a simple and elegant form based on the fact that at resonance, $U^0 = K^0$:

$$\frac{\Delta \omega}{\omega^0} = \frac{1}{2} \left(\frac{\Delta U}{U^0} - \frac{\Delta K}{K^0} \right). \quad (27)$$

Before proceeding to introduce temperature change, a crucial correction needs to be made. Eq. (26) offers the analytical form based on which frequency shift can be calculated. In the expression, unperturbed strain field interacts with the change in stiffness matrix to give the correction in strain energy. In the case of embedding metal blocks inside SiO_2 plate and vice versa, the perturbation of stiffness matrix, Δc , is comparable with c itself and thus it is no longer a small perturbation. In this scenario, the unperturbed field needs to be expressed using a variable that will remain continuous [31], [32]. Thus (26) needs to be rewritten using the unperturbed stress field T^0 instead of strain field S^0 , which will experience a discontinuity (namely, S is no longer continuous) due to Δc whereas T will remain continuous. Because the velocity field and displacement field will always remain continuous, regardless of material embedding, the other terms in (26) remain correct. The new formula is written as

$$\frac{\Delta \omega}{\omega^0} = \frac{\int_{\Omega} (T^0)^* : \Delta(c^{-1}) : T^0 d\Omega - \int \Delta \rho |\omega^0 u^0|^2 d\Omega}{2 \int_{\Omega} \rho^0 |\omega^0 u^0|^2 d\Omega}, \quad (28)$$

where

$$T^0 = c^0 : \nabla_s u^0, \quad (29)$$

$$\Delta(c^{-1}) = (c^0 + c^1)^{-1} - (c^0)^{-1}. \quad (30)$$

B. Temperature-Induced Frequency Perturbation and TCF

Frequency perturbation due to material property change is derived in the previous section. Because temperature affects the material properties, its influence on the resonant frequency can be derived based on (28).

Temperature-induced density change is ignored for simplicity, thus $\partial\rho/\partial t = 0$. But its effect can be added back to the formulation. To the first order, temperature-induced perturbation can be written as

$$\Delta c = (\partial c/\partial t)\Delta t, \quad (31)$$

$$\Delta\omega = (\partial\omega/\partial t)\Delta t, \quad (32)$$

where t represents temperature.

Substituting back into (28) and applying chain rule, one finds:

$$\frac{\partial\omega/\partial t}{\omega^0} = \frac{\int_{\Omega}(T^0)^*: [(c^0)^{-2}\frac{\partial c}{\partial t}]: T^0 d\Omega}{2\int_{\Omega}\rho^0|\omega^0 u^0|^2 d\Omega}. \quad (33)$$

Notice that the superscript 0 denotes unperturbed fields and resonant frequency at the reference temperature, namely, room temperature. But this unperturbed field should already have been affected by the embedded compensating material because we are now dealing with temperature perturbation on top of perturbation due to material embedding.

For simplicity, an isotropic material is chosen in which every element in the stiffness matrix c is proportional to Young's modulus E . Thus $\partial c/\partial t$ can be written as

$$\frac{\partial c/\partial t}{c} = \frac{\partial E/\partial t}{E} \rightarrow \partial c/\partial t = \frac{\partial E/\partial t}{E} c = \text{TCE} \cdot c. \quad (34)$$

As a result (33) can be written as

$$\frac{\partial\omega/\partial t}{\omega^0} = \frac{\int_{\Omega}\text{TCE} \cdot (T^0)^*: [(c^0)^{-1}]: T^0 d\Omega}{2\int_{\Omega}\rho^0|\omega^0 u^0|^2 d\Omega}. \quad (35)$$

On the left side of (35), $(\partial\omega/\partial t)/\omega^0$ is simply the definition of temperature coefficient of frequency (TCF). Thus the TCF of the resonator can be expressed as

$$\text{TCF} = \frac{\int_{\Omega}\text{TCE} \cdot (T^0)^*: [(c^0)^{-1}]: T^0 d\Omega}{2\int_{\Omega}\rho^0|\omega^0 u^0|^2 d\Omega}, \quad (36)$$

$$\text{TCF} = \frac{\int_{\Omega}\text{TCE} \cdot U^0(\vec{r}) d\Omega}{2K^0}, \quad (37)$$

where $U^0(\vec{r})$ is the strain energy density at location \vec{r} , and K^0 is the total kinetic energy of the resonator.

This is an important and powerful result which gives an analytical model for calculating the TCF of any MEMS

resonator with arbitrary mode shape, as long as its material properties and configuration and its unperturbed (room temperature) mode shape are known. The method works for both in-plane and out-of-plane resonant modes.

For MEMS resonator made of homogeneous material, the TCE term can be pulled outside the integral and due to equal partition of kinetic energy and strain energy at resonance, $\text{TCF} = 1/2 \cdot \text{TCE}$. For MEMS resonator made of composite material, each material TCE is weighted by the local strain energy density, namely the part of resonator that has larger strain energy concentration is more powerful in determining the TCF of the entire device through its local TCE. If the device is made of several domains of homogeneous material, such as metal blocks embedded in an oxide plate, the above equation can be rewritten as

$$\text{TCF} = \frac{\int_{\Omega}\text{TCE}_i \cdot U_i^0 d\Omega}{2K^0}, \quad (38)$$

where subscript i represents the i th homogeneous domain.

In conventional TCF analysis, resonant frequency needs to be calculated at various temperatures and its change versus temperature gives the TCF. For resonating structures that do not have free boundaries, namely, resonators that are anchored throughout their perimeter or fully connected to the substrate, eigenfrequency simulation often fails to distinguish the frequencies of the desired resonant mode because the mode extends to the entire wafer or substrate, and perfectly matched layers (PMLs) are often necessary. As a result, time-consuming frequency domain sweeps have to be performed to locate resonance peak accurately. The above result offers a quick and intuitive analytical approach to derive the first-order TCF of any MEMS resonator, given its unperturbed (or, room-temperature) mode shape, which only needs to be computed once and may also be approximated in analytical form. This approach helps designers choose the ideal location to place thermal stability compensation blocks without time-consuming simulation.

C. Combining Material Embedding With Temperature Change

So far two types of perturbations have been introduced—structural perturbation due to material embedding and thermal perturbation due to temperature change. Strictly speaking the unperturbed field in (36) is the perturbed field after structural perturbation, thus it is not the same as that in (28). In practice, the unperturbed field before structural perturbation, namely the mode in homogeneous material [as in (28)], can be used in (36) without introducing too much error, as will be shown in Section III. The reasoning behind is that the change in stiffness Δc and change in density $\Delta\rho$ can be broken up into contributions from temperature change and changes in material due to material embedding. When all of these compo-

nents yield small effects, they can be lumped into a single perturbation that results in a small change in frequency. In this case, knowing the mode shape of the homogeneous resonator at room temperature suffices to give the frequency shift due to both structural perturbation (material embedding) and thermal perturbation (temperature change). The mode shape for a homogeneous resonator is often easy to simulate, approximate, or may even be available in analytical form. On the other hand, if material embedding leads to significant change or better accuracy is needed, the mode shape after structural perturbation, namely, mode shape of the composite resonator, should be used in (36).

III. COMPARISON WITH FINITE ELEMENT METHOD (FEM) SIMULATION

In this section, the proposed analytical model is implemented to determine the TCF of a multilayer CMOS-MEMS composite material Lamé mode bulk acoustic resonator. A step-by-step guide is given and the results are compared with COMSOL finite element simulation results, showing good matching between the analytical approach and simulation.

A. Unperturbed Mode Shape

Because the resonator side length is much larger than its thickness, the displacement field is assumed to be independent of height, and can be written as [33]

$$u_x = \sin(kx)\cos(ky), \quad (39)$$

$$u_y = -\cos(kx)\sin(ky). \quad (40)$$

As a result, the strain field can be derived using the following relationship:

$$S_x = \frac{\partial u_x}{\partial x}, \quad (41)$$

$$S_y = \frac{\partial u_y}{\partial y}, \quad (42)$$

$$S_{xy} = \frac{\partial u_x}{\partial y} + \frac{\partial u_y}{\partial x}. \quad (43)$$

With the above result and using plane stress approximation, the stress field distribution can be calculated:

$$T_x = \frac{E}{1-\nu^2}(S_x + \nu S_y), \quad (44)$$

$$T_y = \frac{E}{1-\nu^2}(\nu S_x + S_y), \quad (45)$$

$$T_{xy} = \frac{E}{2(1+\nu)}S_{xy}, \quad (46)$$

where E is the Young's Modulus and ν is the Poisson ratio.

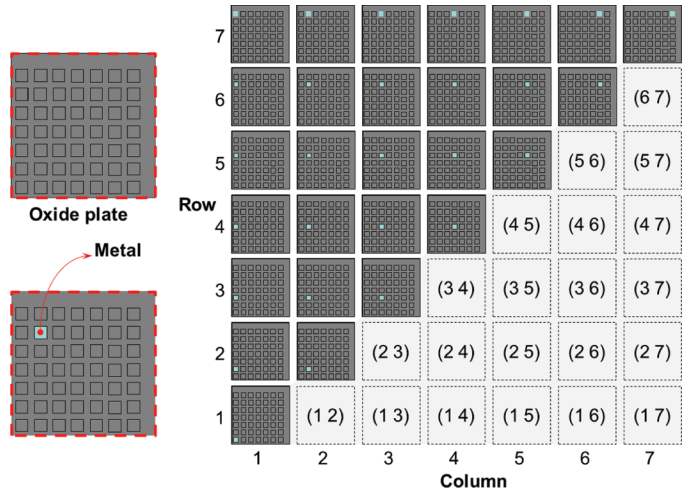


Fig. 4. Test structure to benchmark the analytical model with FEM simulation. It has a 7×7 place holder for material embedding. Only the first quadrant of the plate is shown, due to symmetry of the Lamé mode.

Since this is essentially a 2-D mode, the 6 by 1 stress and strain vectors (T and S) can be simplified into 3 by 1 vectors, which only have x , y , and xy components. The stiffness matrix c can also be simplified. Thus,

$$T = c : S, \quad (47)$$

$$\begin{bmatrix} T_x \\ T_y \\ T_{xy} \end{bmatrix} = \begin{bmatrix} \frac{E}{1-\nu^2} & \frac{E\nu}{1-\nu^2} & 0 \\ \frac{E\nu}{1-\nu^2} & \frac{E}{1-\nu^2} & 0 \\ 0 & 0 & \frac{E}{1+2\nu} \end{bmatrix} \begin{bmatrix} S_x \\ S_y \\ S_{xy} \end{bmatrix}. \quad (48)$$

B. Single Layer Frequency Shift Due to Material Embedding

Based on the unperturbed mode shape and the analytical model, as expressed in (28), the resonant frequency shift of a single layer can be calculated. The analytical model is tested using the structure shown in Fig. 4, which allows temperature compensating blocks to be placed at different locations on the homogeneous SiO_2 plate. A 7×7 placeholder is created, and (i,j) indicates that the temperature compensating block is put in the slot at the intersection between the i th row and j th column in the grid. For simplicity, only the first quadrant of the structure is shown due to mode symmetry (inset of Fig. 1). The results of adding metal compensating blocks to the oxide-based plate (mat.2) are shown and analyzed in this section. Embedding oxide blocks inside metal-based plate (mat.1) yields similar results with comparable accuracy, except that the trend is opposite, because the TCEs of aluminum and SiO_2 have opposite signs.

Fig. 5 shows the resonant frequency shift at room temperature due to metal embedding at different locations in the test structure. Because the mode shape is symmetric around the plate diagonal, the effects of blocks placed at (i,j) and (j,i) are identical. In places where aluminum

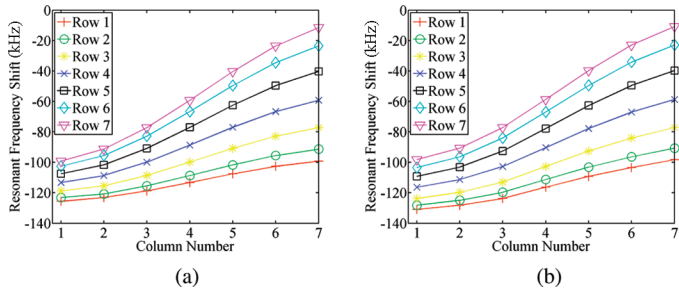
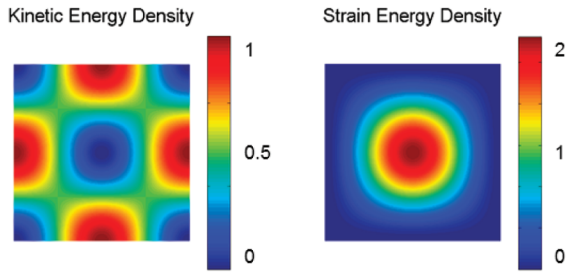


Fig. 5. Resonant frequency shift of a single layer SiO_2 plate due to a single block of metal embedded at various locations. Comparison between (a) FEM simulation and (b) analytical model shows good accuracy. The unperturbed resonance frequency is 56.81 MHz. Maximum frequency shift is 0.26%.

replaces SiO_2 , the strain energy density decreases due to a larger Poisson ratio and the kinetic energy density increases due to a higher density. This leads to $\Delta U < 0$ and $\Delta K > 0$, and consequently resonance frequency drops according to (27). It is found that row 1 is almost flat. This means blocks placed at row 1 cause very similar frequency shift regardless of their corresponding column locations. This can be verified from the potential and kinetic energy density distributions in the unperturbed resonator, shown in Fig. 6. At location (1,1), strain energy density is large and kinetic energy density is small; at location (1,7), kinetic energy density becomes large and strain energy density becomes small. Consequently at location (1,1), the frequency drop is mainly due to strain energy decrease, whereas at location (1,7), the frequency drop is mainly due to kinetic energy increase. The contributions from ΔU and ΔK shift weight in the middle, but their combined contribution remains more or less the same, leading to the weak column position dependency of row 1. In contrast, in row 7, column position has stronger effect on the frequency shift, because strain energy density remains negligible along the entire row but kinetic energy density drops significantly from (7,1) to (7,7), leading to a stronger column dependence. Column dependence gradually increases when transitioning from row 1 to row 7.



	Density	Poisson Ratio	Young's Modulus	TCE
Al	2700 kg/m ³	0.35	70GPa	185ppm/K
SiO_2	2200 kg/m ³	0.17	70GPa	-739ppm/K

Fig. 6. Kinetic and strain energy density of the Lamé mode. Material properties of aluminum and SiO_2 are also shown. The color bar indicates relative energy density normalized to the maximum kinetic energy density.

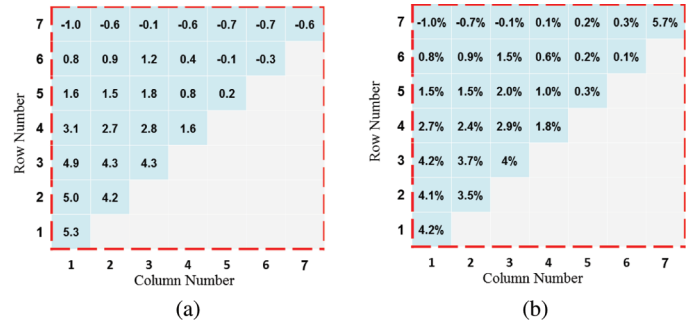


Fig. 7. (a) Difference between frequency shifts predicted by the FEM simulation and the analytical model, in kilohertz, and (b) the percentage error, when the metal compensating block is placed at different locations on the oxide plate. The unperturbed resonant frequency is 56.81 MHz.

Fig. 7 shows that the analytical model can accurately predict the resonance frequency shift due to material embedding at various locations and thus offers intuition on how the frequency shift relates to embedding location and material properties. In practice, more than one block will be embedded into the plate. Table I shows that the analytical model remains accurate even when multiple compensating slots are used. The analytical model is capable of predicting the resonant frequency shift due to material embedding within 7% accuracy. Thus the weighting factors A and B in (1) can be calculated based on the new resonant frequency of mat.1 and mat.2. However, to derive the overall TCF of the multilayer structure, single layer TCFs must be calculated.

C. Single Layer TCF

In this section, (36) is applied to calculate the single layer TCF. Though this is only an approximation, the same unperturbed stress field as that used in the previous section, namely the field of a homogeneous plate, will be used as T^0 in (36). Using the same test structure as shown in Fig. 4, the single layer TCFs due to material embedding at one single slot are shown in Fig. 8. Fig. 9 shows the error between the FEM simulation and the analytical model. A maximum percentage error of 2.2% occurs when the compensating block is at the center of the plate, namely at location (1,1). In practice more than one compensating block will be embedded into the single layer. Table II

TABLE I. COMPARISON BETWEEN FEM SIMULATION AND ANALYTICAL MODEL IN DETERMINING RESONANCE FREQUENCY WHEN MULTIPLE COMPENSATING ALUMINUM BLOCKS ARE EMBEDDED IN A SiO_2 PLATE.

Resonant frequency = 56.81 MHz					
Frequency shift FEM (MHz)	-0.50	-1.08	-2.29	-1.80	-1.96
Frequency shift analytical model (MHz)	-0.51	-1.11	-2.38	-1.86	-2.08
Error (%)	2	2.7	3.9	3.3	6.1

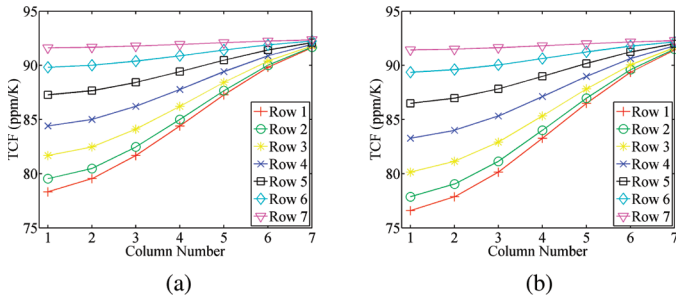


Fig. 8. Oxide-based single layer TCF due to a single block metal embeded at different locations in the Lamé mode resonator. (a) FEM, (b) analytical model.

compares the results calculated based on (36) and those calculated from FEM simulation.

The error is due to the fact that stress field T^0 of the homogeneous plate, instead of that of the composite plate, is used in calculating the TCF according to (36). An easy remedy is to numerically simulate the mode shape of the composite plate including the compensating material embedded and then use this more accurate mode shape as the unperturbed field in (36). Fig. 10 shows the TCF due to a single embedded block using this semi-analytical approach and the model matches full-blown FEM simulation within 0.3% at the maximum error location. Table III shows a comparison between the semi-analytical approach and the FEM simulation using different compensating configurations with multiple compensating blocks involved. Improved accuracy can be observed by comparing Fig. 11 with Fig. 9 and Table III with Table II.

D. Multilayer Resonator With Sub-ppm TCF

Previous steps have demonstrated the procedure and result for calculating the frequency shift and TCF of a single layer of the composite Lamé-mode resonator. For a CMOS-MEMS multilayer resonator, all the variables necessary to evaluate (1) have been derived.

In contrast to the pure oxide plate, mat.1 and mat.2 plates offer great design flexibility in terms of position and number of embedded compensating blocks. The analytical mode offers a quick way to independently tune each plate

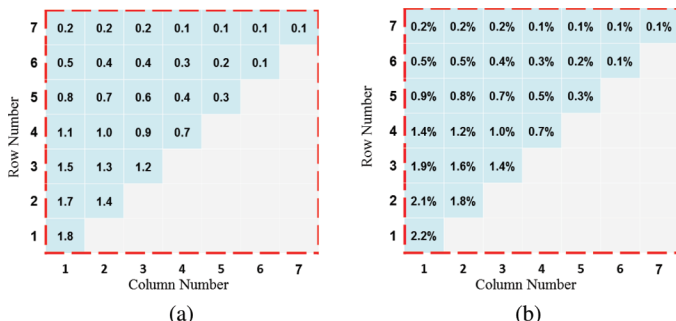


Fig. 9. (a) Difference in ppm/K, and (b) percentage error in TCF between the FEM simulation and the analytical model, and the percentage error, when a single metal compensating block is placed at different locations on the oxide plate.

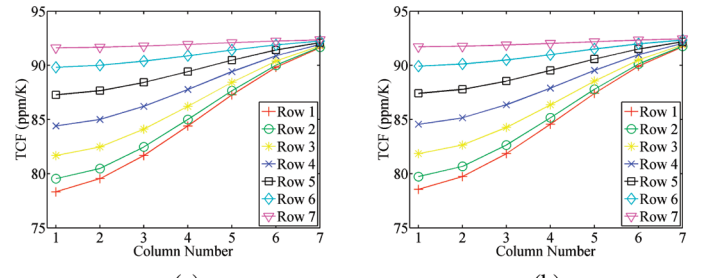


Fig. 10. Oxide-based single layer TCF due to single metal embedding at different test locations. (a) FEM, (b) Analytical model.

to achieve the overall thermal stability of the multilayer structure. This method offers an efficient and intuitive method for coarse tuning of the multilayer structures to achieve a small TCF. Table IV lists the design after coarse tuning. The material configuration, room temperature resonant frequency and TCF for each type of plate are included. Because the goal is to achieve highly thermally stable resonator with sub-ppm TCF, the semi-analytical approach is used to calculate the TCF of each individual layer to reduce approximation error. In spite of this, there will still be error involved in deriving the multilayer TCF based on each individual layer. Consequently, this approach works best for coarse tuning to get the TCF to a reasonably small value: 3.04 ppm/K for this design.

As a next step, fine tuning is required to achieve sub-ppm temperature stability. For a given multilayer material configuration, its TCF can be derived by simply performing one single eigenfrequency simulation on the entire structure to calculate the mode shape of the composite material resonator and then use (36) to derive the overall TCF. This method fits better for fine tuning the material embedding to achieve sub-ppm TCF. Intuition gained from the previous step can help in determining where to embed more compensating material or which block to take out. Using this method, the first-order TCF is improved to -0.22 ppm/K, a level within the design requirement. The design is shown in Table V. There is a slight modification in the mat.1 plate after fine tuning. As a validation, FEM simulation predicts a first-order TCF of -0.28 ppm/K at room temperature on the final design, matching closely to the analytical model. As can be seen from Fig. 12, frequency shift becomes mostly a quadratic function of the temperature after the linear TCF has been successfully compensated. The second order TCF is -0.007 ppm/K².

TABLE II. TCF OF A SINGLE-LAYER OXIDE PLATE DUE TO METAL EMBEDDING AT MULTIPLE LOCATIONS.

TCF FEM (ppm/K)	39.59	-11.76	-79.37	-58.25	-103.28
TCF analytical model (ppm/K)	37.47	-15.53	-88.80	-65.48	-118.47
Error (%)	5.4	32.1	11.9	12.4	14.7

TABLE III. TCF OF A SINGLE-LAYER OXIDE PLATE DUE TO METAL EMBEDDED AT MULTIPLE LOCATIONS USING THE SEMI-ANALYTICAL APPROACH.

TCF FEM (ppm/K)	39.59	-11.76	-79.37	-58.25	-103.28
TCF analytical model (ppm/K)	40.15	-10.86	-78.37	-57.23	-102.34
Error (%)	1.4	7.7	1.3	1.8	0.9

In general, after coarse tuning only a few fine tuning steps are required to further reduce the TCF to sub-ppm level.

Finally, anchor beams, Tungsten electrodes, and oxide edge for etching protection are added to fully represent a real device. The above design can be re-tuned to achieve a TCF of -0.21 ppm/K, according to FEM simulation, after adding all these extra elements. The final design is shown in Table VI.

IV. APPLICATION IN NUMERICAL SIMULATION PACKAGES

As demonstrated in the previous section, the analytical model provides a way to efficiently predict and simulate the first-order TCF of a composite resonant structure. In general, this model can be applied in two different scenarios.

In the case where structures for which eigenmode simulation is easy, first-order TCF can be calculated by performing two eigenmode simulations at two nearby temperatures, respectively, and calculating the fractional change between the two eigenfrequencies per unit degree of temperature change. In this case, the aforementioned analytical model can simplify the calculation to only one single eigenmode simulation. Furthermore, this model allows the designer to use the unperturbed mode shape and get real-time update of an estimated TCF while moving the temperature compensating blocks to different locations inside

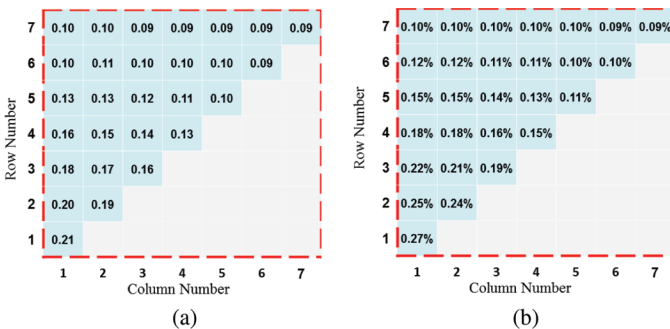


Fig. 11. (a) Difference in ppm/K and (b) percentage error in TCF between the FEM simulation and the analytical model, when the compensating block is placed at different locations in the test structure. Increased accuracy is demonstrated in comparison with Fig. 9, for an unperturbed mode shape based on FEM simulation (semi-analytical approach).

TABLE IV. TEMPORARY DESIGN AFTER COARSE TUNING.

Embedding configuration	Resonant frequency (MHz)	TCF (ppm/K)	Number of plates	Plate height (μm)	Effective density (kg/m³)
Oxide	56.81	92.50	5	0.85	2200.00
mat.1	49.50	-286.53	2	0.53	2561.57
metal with oxide					
mat.2	52.86	-106.41	2	0.53	2384.89
oxide with metal					

Predicted TCF is 3.04 ppm/K according to (1).

the structure to coarse tune the thermal stability. This allows for intuitive and interactive design experience when integrated within numerical simulation packages.

The second case is when designers are trying to predict the TCF of a resonant structure, but it is difficult to perform the eigenmode simulation of that structure. Such a challenge is common for unreleased structures, such as unreleased CMOS-MEMS resonators [34], SAW resonators [35], and resonators that are anchored on the entire perimeter, for example, a phononic crystal resonator [36]. In such cases, the analytical model becomes particularly useful because it only requires an approximate mode shape, and thus no time-consuming frequency sweep is required to accurately resolve the resonant frequency and resonant mode. The designer can first perform a coarse frequency sweep around the resonance and pick a displacement field at a frequency close to the resonance. The TCF formula (36) needs slight modification in this case, because the kinetic energy and strain energy are not equal at off-resonance frequencies. The expression for TCF using off-resonance field is

$$\text{TCF} = \frac{\int_{\Omega} \text{TCE} \cdot (T^0)^* : [(c^0)^{-1}] : T^0 d\Omega}{2 \int_{\Omega} (T^0)^* : [(c^0)^{-1}] : T^0 d\Omega}, \quad (49)$$

$$\text{TCF} = \frac{\int_{\Omega} \text{TCE} \cdot U^0(\vec{r}) d\Omega}{2U^0}, \quad (50)$$

where T^0 and U^0 are stress field and total strain energy evaluated near the resonance, but not at the exact resonance frequency.

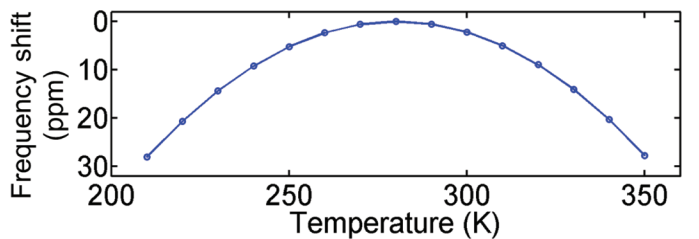


Fig. 12. Frequency shift vs temperature after the fine tuning. Quadratic dependency is dominant, showing good first-order TCF compensation.

TABLE V. CMOS-MEMS RESONATOR DESIGN THAT ACHIEVES A SUB-PPM FIRST-ORDER TCF OF -0.28 ppm/K .

Oxide		mat.1 metal with oxide		mat.2 oxide with metal	
-------	--	---------------------------------	--	---------------------------------	--

Fig. 13 shows the TCF calculated using the analytical model, based on the displacement field at various frequencies close to the resonance. Both the modified formulation and the unmodified formulation deviate from the TCF obtained from FEM simulation, due to the error inherent in the first-order perturbation theory when the perturbation is no longer infinitesimally small. But as can be seen, the modified formulation that uses strain energy in the denominator gives better consistency compared with the unmodified formulation that uses kinetic energy in the denominator. Even when the frequency is relatively far from the resonance, the predicted TCF based on the off-resonance displacement field is still close to that predicted using the resonant mode shape. Consequently this analytical model remains robust even if the off-resonance displacement field is used, and thus can save tremendous simulation time when used to predict the TCF of a high-quality factor resonator, where a brute force frequency sweep necessitates fine steps to resolve the resonance peak, making the computation costly and time consuming.

V. CONCLUSION

In this work, a CMOS-MEMS resonator design in $0.18 \mu\text{m}$ 1-poly-6-metal standard CMOS process that uses embedded metal block for temperature compensation is proposed and shows sub-ppm temperature stability (-0.21 ppm/K). A comprehensive analytical model is derived and applied to analyze and optimize the TCF of CMOS-MEMS composite material resonators. Comparison with FEM simulation demonstrates good accuracy. The model can also be applied to predict and analyze the TCF of MEMS resonators with arbitrary mode shape, and its integration with simulation packages can enable an interactive and efficient design process.

APPENDIX A TCF OF THE MULTILAYER STRUCTURE AS A COMBINATION OF THE SINGLE-LAYER TCFs

The overall resonance frequency of the multilayer CMOS-MEMS resonator can be written as the linear combination of the resonance frequency of each single-layer plate [37]:

$$f_{\text{total}}^2 = \frac{m_{\text{mat.1}}}{m_{\text{total}}} f_{\text{mat.1}}^2 + \frac{m_{\text{mat.2}}}{m_{\text{total}}} f_{\text{mat.2}}^2 + \frac{m_{\text{oxide}}}{m_{\text{total}}} f_{\text{oxide}}^2. \quad (51)$$

TABLE VI. FINAL DESIGN ACHIEVES -0.21 ppm/K TCF.

Oxide		mat.1 metal with oxide		mat.2 oxide with metal	
-------	--	---------------------------------	--	---------------------------------	--

Anchor beam, Tungsten electrodes, and oxide edge for etching protection have all been considered.

Taking the derivative of (51) with respect to temperature t and dividing both sides by $2f_{\text{total}}^2$ led to

$$\frac{1}{f_{\text{total}}} \frac{\partial f_{\text{total}}}{\partial t} = \frac{A \cdot \frac{1}{f_{\text{mat.1}}} \frac{\partial f_{\text{mat.1}}}{\partial t} + B \cdot \frac{1}{f_{\text{mat.2}}} \frac{\partial f_{\text{mat.2}}}{\partial t} + C \cdot \frac{1}{f_{\text{oxide}}} \frac{\partial f_{\text{oxide}}}{\partial t}}{A + B + C}, \quad (52)$$

where

$$A = h_{\text{mat.1}} \rho_{\text{mat.1}} f_{\text{mat.1}}^2, \quad (53)$$

$$B = h_{\text{mat.2}} \rho_{\text{mat.2}} f_{\text{mat.2}}^2, \quad (54)$$

$$C = h_{\text{ox}} \rho_{\text{ox}} f_{\text{ox}}^2. \quad (55)$$

ρ_{mat} is the effective density of that plate, which can be calculated using the average density in the plate weighted by the local displacement squared:

$$\rho_{\text{mat}} = \frac{\int_{\Omega} \rho(x, y) u^2(x, y) d\Omega}{\int_{\Omega} u^2(x, y) d\Omega}. \quad (56)$$

From this the expression of the TCF of a multilayer structure can be derived:

$$\text{TCF} = \frac{A \cdot \text{TCF}_{\text{mat.1}} + B \cdot \text{TCF}_{\text{mat.2}} + C \cdot \text{TCF}_{\text{ox}}}{A + B + C}. \quad (57)$$

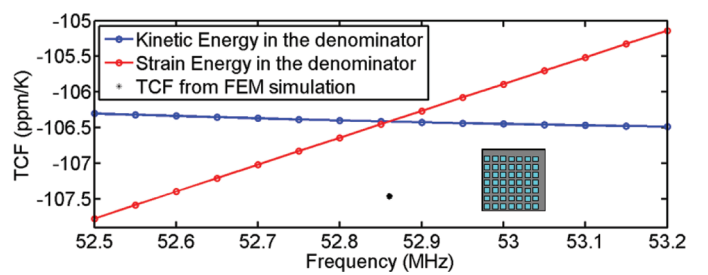


Fig. 13. TCF from analytical model, using off-resonance mode shapes evaluated at different frequencies near the resonance. The inset shows the structure, based on which the simulation is done. The modified formula uses strain energy in the denominator as in (50), whereas the unmodified formula uses kinetic energy in the denominator as in (37).

APPENDIX B
PROPERTY OF STRAIN DISPLACEMENT OPERATOR ∇_s
AND DIVERGENCE OPERATOR ∇ .

The results to be proved are the following:

$$\langle \nabla_s u | T \rangle = \langle -u | \nabla \cdot T \rangle, \quad (58)$$

$$\langle T | \nabla_s u \rangle = \langle -\nabla \cdot T | u \rangle. \quad (59)$$

Here, u is the displacement field, T is the stress field, and operator $\nabla \cdot$ and ∇_s are defined in Section II of this paper. Because these two identities are equivalent, only the proof for the first one is provided.

The right hand side of (58), without the minus sign, can be written as

$$\begin{aligned} & \langle u | \nabla \cdot T \rangle = \\ & \left\langle \begin{bmatrix} u_x \\ u_y \\ u_z \end{bmatrix} | \begin{bmatrix} \partial/\partial x & 0 & 0 & 0 & \partial/\partial z & \partial/\partial y \\ 0 & \partial/\partial y & 0 & \partial/\partial z & 0 & \partial/\partial x \\ 0 & 0 & \partial/\partial z & \partial/\partial y & \partial/\partial x & 0 \end{bmatrix} \begin{bmatrix} T_{xx} \\ T_{xy} \\ T_{yy} \\ T_{yz} \\ T_{zx} \\ T_{xy} \end{bmatrix} \right\rangle \\ &= \int_{\Omega} u_x^* \left(\frac{\partial T_{xx}}{\partial x} + \frac{\partial T_{xy}}{\partial y} + \frac{\partial T_{xz}}{\partial z} \right) \\ &+ \int_{\Omega} u_y^* \left(\frac{\partial T_{xy}}{\partial x} + \frac{\partial T_{yy}}{\partial y} + \frac{\partial T_{yz}}{\partial z} \right) \\ &+ \int_{\Omega} u_z^* \left(\frac{\partial T_{xz}}{\partial x} + \frac{\partial T_{yz}}{\partial y} + \frac{\partial T_{zz}}{\partial z} \right). \end{aligned} \quad (60)$$

Using the vector identity

$$\operatorname{div}(\psi \vec{A}) = \psi \cdot \operatorname{div}(\vec{A}) + \operatorname{grad}(\psi) \cdot \vec{A}, \quad (61)$$

where \vec{A} is a vector field and ψ is a scalar field, the above equations can be rewritten as

$$\begin{aligned} & \langle u | \nabla \cdot T \rangle = \\ & \int_{\Omega} \operatorname{div} \left(u_x^* \cdot \begin{bmatrix} T_{xx} \\ T_{xy} \\ T_{xz} \end{bmatrix} \right) d\Omega + \int_{\Omega} \operatorname{div} \left(u_y^* \cdot \begin{bmatrix} T_{xy} \\ T_{yy} \\ T_{yz} \end{bmatrix} \right) d\Omega \\ & \int_{\Omega} \operatorname{div} \left(u_z^* \cdot \begin{bmatrix} T_{xz} \\ T_{yz} \\ T_{zz} \end{bmatrix} \right) d\Omega - \int_{\Omega} \operatorname{grad}(u_x^*) \cdot \begin{bmatrix} T_{xx} \\ T_{xy} \\ T_{xz} \end{bmatrix} d\Omega - \\ & \int_{\Omega} \operatorname{grad}(u_y^*) \cdot \begin{bmatrix} T_{yx} \\ T_{yy} \\ T_{yz} \end{bmatrix} d\Omega - \int_{\Omega} \operatorname{grad}(u_z^*) \cdot \begin{bmatrix} T_{zx} \\ T_{zy} \\ T_{zz} \end{bmatrix} d\Omega. \end{aligned} \quad (62)$$

Then Gauss's law is applied to the divergence terms to change the volume integrals into surface integrals, where $\partial\Omega$ denotes the surface of Ω .

$$\begin{aligned} \langle u | \nabla \cdot T \rangle &= \int_{\partial\Omega} u_x^* \cdot \begin{bmatrix} T_{xx} \\ T_{xy} \\ T_{xz} \end{bmatrix} \cdot \vec{n} dA + \int_{\partial\Omega} u_y^* \cdot \begin{bmatrix} T_{xy} \\ T_{yy} \\ T_{yz} \end{bmatrix} \cdot \vec{n} dA + \\ &\quad \int_{\partial\Omega} u_z^* \cdot \begin{bmatrix} T_{xz} \\ T_{yz} \\ T_{zz} \end{bmatrix} \cdot \vec{n} dA - \int_{\Omega} \operatorname{grad}(u_x^*) \cdot \begin{bmatrix} T_{xx} \\ T_{xy} \\ T_{xz} \end{bmatrix} d\Omega - \\ &\quad \int_{\Omega} \operatorname{grad}(u_y^*) \cdot \begin{bmatrix} T_{yx} \\ T_{yy} \\ T_{yz} \end{bmatrix} d\Omega - \int_{\Omega} \operatorname{grad}(u_z^*) \cdot \begin{bmatrix} T_{zx} \\ T_{zy} \\ T_{zz} \end{bmatrix} d\Omega. \end{aligned} \quad (63)$$

For a freely suspended resonator of finite size, the surface integrals are zero because stress along the surface normal \vec{n} has to be zero at a free boundary. For an unreleased resonator or a resonator anchored on the entire perimeter, the mode is localized [36] and the domain surface $\partial\Omega$ can be extended to infinity, where the stress and strain field are infinitesimally small. The surface integral also goes to zero in this scenario. Thus,

$$\begin{aligned} \langle u | \nabla \cdot T \rangle &= - \int_{\Omega} \operatorname{grad}(u_x^*) \cdot \begin{bmatrix} T_{xx} \\ T_{xy} \\ T_{xz} \end{bmatrix} d\Omega - \\ &\quad \int_{\Omega} \operatorname{grad}(u_y^*) \cdot \begin{bmatrix} T_{yx} \\ T_{yy} \\ T_{yz} \end{bmatrix} d\Omega - \int_{\Omega} \operatorname{grad}(u_z^*) \cdot \begin{bmatrix} T_{zx} \\ T_{zy} \\ T_{zz} \end{bmatrix} d\Omega. \end{aligned} \quad (64)$$

As for the left-hand side,

$$\begin{aligned} \langle \nabla_s u | T \rangle &= \left\langle \begin{bmatrix} \partial \partial x & 0 & 0 \\ 0 & \partial \partial y & 0 \\ 0 & 0 & \partial \partial z \end{bmatrix} \begin{bmatrix} u_x \\ u_y \\ u_z \end{bmatrix} | \begin{bmatrix} T_{xx} \\ T_{yy} \\ T_{zz} \\ T_{yz} \\ T_{zx} \\ T_{xy} \end{bmatrix} \right\rangle \\ & \langle \nabla_s u | T \rangle = \int_{\Omega} \left(\frac{\partial u_x^*}{\partial x} T_{xx} + \frac{\partial u_x^*}{\partial y} T_{xy} + \frac{\partial u_x^*}{\partial z} T_{xz} \right) d\Omega \\ &+ \int_{\Omega} \left(\frac{\partial u_y^*}{\partial x} T_{yx} + \frac{\partial u_y^*}{\partial y} T_{yy} + \frac{\partial u_y^*}{\partial z} T_{yz} \right) d\Omega \\ &+ \int_{\Omega} \left(\frac{\partial u_z^*}{\partial x} T_{zx} + \frac{\partial u_z^*}{\partial y} T_{zy} + \frac{\partial u_z^*}{\partial z} T_{zz} \right) d\Omega. \end{aligned} \quad (65)$$

It can be further simplified into the following form:

$$\begin{aligned} \langle \nabla_s u | T \rangle &= \int_{\Omega} \operatorname{grad}(u_x^*) \cdot \begin{bmatrix} T_{xx} \\ T_{xy} \\ T_{xz} \end{bmatrix} + \\ &\quad \int_{\Omega} \operatorname{grad}(u_y^*) \cdot \begin{bmatrix} T_{yx} \\ T_{yy} \\ T_{yz} \end{bmatrix} + \int_{\Omega} \operatorname{grad}(u_z^*) \cdot \begin{bmatrix} T_{zx} \\ T_{zy} \\ T_{zz} \end{bmatrix}. \end{aligned} \quad (66)$$

Now it becomes obvious that

$$\langle \nabla_s u | T \rangle = - \langle u | \nabla \cdot T \rangle. \quad (67)$$

APPENDIX C HERMITICITY OF \hat{A} AND \hat{B}

$\hat{B} = \rho$, thus it is trivial to show that \hat{B} is Hermitian because ρ is real and consequently

$$\langle \rho u | u \rangle = \langle u | \rho u \rangle. \quad (68)$$

As for $\hat{A} = -\nabla \cdot c : \nabla_s$, proving it is hermitian requires applying the conclusion from Appendix B twice. First, the divergence operator $\nabla \cdot$ is moved to the left side of the inner product:

$$\langle u | \hat{A} u \rangle = \langle u | -\nabla \cdot c : \nabla_s u \rangle = \langle \nabla_s u | c : \nabla_s u \rangle. \quad (69)$$

Then the stiffness matrix c and operator ∇_s are moved to the left side:

$$\langle u | \hat{A} u \rangle = \langle \nabla_s \cdot u | c : \nabla_s u \rangle = \langle -\nabla \cdot c : \nabla_s u | u \rangle. \quad (70)$$

This proves $\hat{A} = -\nabla \cdot c : \nabla_s$ is also a Hermitian operator.

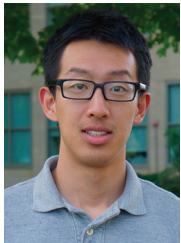
ACKNOWLEDGMENTS

The authors thank Professor S. Johnson from MIT and Taiwan Semiconductor Manufacturing Company (TSMC) for helpful discussion.

REFERENCES

- [1] *Sit8208 Datasheets*. SiTime Inc., Sunnyvale, CA, USA.
- [2] A. Partridge, H.-C. Lee, P. Hagelin, and V. Menon, "We know that MEMS is replacing quartz. But why? And why now?" in *2013 Joint European Frequency and Time Forum Int. Frequency Control Symp.*, Jul. 2013, pp. 411–416.
- [3] W.-T. Hsu, "Recent progress in silicon MEMS oscillators," tech. rep., DTIC Document, 2008.
- [4] *DSC1001 Datasheets*. Discera Inc., San Jose, CA, USA.
- [5] W. Shockley, D. R. Curran, and D. J. Koneval, "Trapped energy modes in quartz filter crystals," *J. Acoust. Soc. Am.*, vol. 41, no. 4B, pp. 981–993, 1967.
- [6] J. R. Vig, "Quartz crystal resonators and oscillators for frequency control and timing applications. A tutorial," *NASA STI/Recon Technical Report N*, vol. 95, p. 19519, 1994.
- [7] T. Morita, Y. Watanabe, M. Tanaka, and Y. Nakazawa, "Wideband low loss double mode SAW filters," in *Proc. IEEE Ultrasonics Symp.*, vol. 1, Oct. 1992, pp. 95–104.
- [8] R. Ruby, P. Bradley, Y. Oshmyansky, A. Chien, and I. Larson, J.D., "Thin film bulk wave acoustic resonators (FBAR) for wireless applications," in *2001 IEEE Ultrasonics Symp.*, vol. 1, pp. 813–821.
- [9] M. Shalaby, M. Abdelmoneum, and K. Saitou, "Design of spring coupling for high-q high-frequency MEMS filters for wireless applications," *IEEE Trans. Ind. Electron.*, vol. 56, no. 4, pp. 1022–1030, 2009.
- [10] M. F. Zaman, A. Sharma, and F. Ayazi, "High performance matched-mode tuning fork gyroscope," in *19th IEEE Int. Conf. on Micro Electro Mechanical Systems*, 2006, pp. 66–69.
- [11] D. Serrano, R. Tabrizian, and F. Ayazi, "Tunable piezoelectric MEMS resonators for real-time clock," in *2011 Joint Conf. IEEE Int. Frequency Control and the European Frequency and Time Forum*, pp. 1–4.
- [12] S. Asl, S. Mukherjee, W. Chen, K. Joo, R. Palwai, N. Arumugam, P. Galle, M. Phadke, C. Grosjean, J. Salvia, H. Lee, S. Pamarti, T. Fiez, K. Makinwa, A. Partridge, and V. Menon, "12.9 A 1.55 × 0.85mm² 3ppm 1.0μA 32.768khz MEMS-based oscillator," in *2014 IEEE Int. Solid-State Circuits Conf. Dig. of Tech. Papers*, pp. 226–227.
- [13] J. Verd, A. Uranga, J. Teva, J. Lopez, F. Torres, J. Esteve, G. Abadal, F. Perez-Murano, and N. Barniol, "Integrated CMOS-MEMS with on-chip readout electronics for high-frequency applications," *IEEE Electron Device Lett.*, vol. 27, no. 6, pp. 495–497, 2006.
- [14] F. Chen, J. Brotz, U. Arslan, C.-C. Lo, T. Mukherjee, and G. K. Fedder, "CMOS-MEMS resonant RF mixer-filters," in *18th IEEE Int. Conf. on Micro Electro Mechanical Systems*, 2005, pp. 24–27.
- [15] W.-C. Chen, W. Fang, and S.-S. Li, "A generalized CMOS-MEMS platform for micromechanical resonators monolithically integrated with circuits," *J. Micromech. Microeng.*, vol. 21, no. 6, art. no. 065012, 2011.
- [16] J. Lopez, J. Verd, J. Teva, G. Murillo, J. Giner, F. Torres, A. Uranga, G. Abadal, and N. Barniol, "Integration of rf-mems resonators on submicrometric commercial CMOS technologies," *J. Micromech. Microeng.*, vol. 19, no. 1, art. no. 015002, 2009.
- [17] C.-S. Li, L.-J. Hou, and S.-S. Li, "Advanced CMOS-MEMS resonator platform," *IEEE Electron Device Letters*, vol. 33, no. 2, pp. 272–274, 2012.
- [18] W.-C. Chen, W. Fang, and S.-S. Li, "VHF CMOS-MEMS oxide resonators with Q > 10,000," in *2012 IEEE Int. Frequency Control Symp.*, pp. 1–4.
- [19] W.-C. Chen, W. Fang, and S.-S. Li, "High-integrated CMOS-MEMS resonators with deep-submicrometer gaps and quasi-linear frequency tuning," *J. Microelectromech. Syst.*, vol. 21, no. 3, pp. 688–701, 2012.
- [20] W.-T. Hsu and C.-C. Nguyen, "Stiffness-compensated temperature-insensitive micromechanical resonators," in *15th IEEE Int. Conf. on Micro Electro Mechanical Systems*, Jan. 2002, pp. 731–734.
- [21] B. Kim, R. Melamud, M. Hopcroft, S. A. Chandorkar, G. Bahl, M. Messana, R. Candler, G. Yama, and T. Kenny, "Si-SiO₂ composite mems resonators in CMOS compatible wafer-scale thin-film encapsulation," in *2007 Joint IEEE Int. Frequency Control Symp. with the 21st European Frequency and Time Forum*, pp. 1214–1219.
- [22] R. Tabrizian, G. Casinovi, and F. Ayazi, "Temperature-stable silicon oxide (SilOx) micromechanical resonators," *IEEE Trans. Electron Devices*, vol. 60, no. 8, pp. 2656–2663, Aug. 2013.
- [23] V. Thakar and M. Rais-Zadeh, "Temperature-compensated piezoelectrically actuated Lame-mode resonators," in *2014 IEEE 27th Int. Conf. Micro Electro Mechanical Systems*, pp. 214–217.
- [24] A. Samara and F. Ayazi, "Temperature compensation of silicon micromechanical resonators via degenerate doping," in *2009 IEEE Int. Electron Devices Meeting*, pp. 1–4.
- [25] E. Ng, C. Ahn, Y. Yang, V. Hong, C.-F. Chiang, E. Ahadi, M. Ward, and T. Kenny, "Localized, degenerately doped epitaxial silicon for temperature compensation of resonant mems systems," in *2013 Transducers Eurosensors XVII: The 17th Int. Conf. on Solid-State Sensors, Actuators and Microsystems*, pp. 2419–2422.
- [26] T. Pensala, A. Jaakkola, M. Prunnila, and J. Dekker, "Temperature compensation of silicon mems resonators by heavy doping," in *2011 IEEE Int. Ultrasonics Symp.*, pp. 1952–1955.
- [27] M. Hopcroft, R. Melamud, R. N. Candler, W.-T. Park, B. Kim, G. Yama, A. Partridge, M. Lutz, and T. W. Kenny, "Active temperature compensation for micromachined resonators," in *Tech. Dig. Solid-State Sensor, Actuator and Microsystems Workshop*, 2004, pp. 364–367.
- [28] K. Sundaresan, G. Ho, S. Pourkamali, and F. Ayazi, "Electronically temperature compensated silicon bulk acoustic resonator reference oscillators," *IEEE J. Solid-State Circuits*, vol. 42, no. 6, pp. 1425–1434, Jun. 2007.
- [29] G. Ho, K. Sundaresan, S. Pourkamali, and F. Ayazi, "Micromechanical IBARs: Tunable high-q resonators for temperature-compensated reference oscillators," *J. Microelectromech. Syst.*, vol. 19, no. 3, pp. 503–515, Jun. 2010.
- [30] B. A. Auld, *Acoustic Fields and Waves in Solids*, vol. 2, Malabar, FL, USA: Krieger, 1990.
- [31] S. G. Johnson, M. Ibanescu, M. A. Skorobogatiy, O. Weisberg, J. D. Joannopoulos, and Y. Fink, "Perturbation theory for Maxwell's equations with shifting material boundaries," *Phys. Rev. E Stat. Nonlin. Soft Matter Phys.*, vol. 65, no. 6 pt. 2, art. no. 066611, Jun. 2002.
- [32] S. Johnson, M. Povinelli, M. Soljačić, A. Karalis, S. Jacobs, and J. D. Joannopoulos, "Roughness losses and volume-current methods in photonic-crystal waveguides," *Appl. Phys. B*, vol. 81, no. 2–3, pp. 283–293, 2005.
- [33] M. Ziae Moayyed, D. Elata, J. Hsieh, J. W. P. Chen, E. P. Quevy, and R. T. Howe, "Fully differential internal electrostatic transduc-

- tion of a Lame-mode resonator," in *IEEE 22nd Int. Conf. Micro Electro Mechanical Systems*, 2009, pp. 931–934.
- [34] B. Bahr, R. Marathe, W. Wang, and D. Weinstein, "Solid state RF MEMS resonators in standard CMOS," in *2013 Proc. European Solid-State Circuits Conf.*, pp. 249–252.
- [35] M. Faucher, G. Martin, J.-M. Friedt, and S. Ballandras, "A 1 GHZ SAW oscillator on epitaxial GaN/Si substrate: Toward co-integrated frequency sources," in *2013 Joint European Frequency and Time Forum Int. Frequency Control Symp.*, pp. 21–24.
- [36] S. Wang, L. Popa, and D. Weinstein, "GaN MEMS resonator using a folded phononic crystal structure," in *Solid-State Sensors, Actuators, and Microsystems*, 2014, pp. 72–75.
- [37] R. Melamud, S. A. Chandorkar, B. Kim, H. K. Lee, J. Salvia, G. Bahl, M. Hopcroft, and T. Kenny, "Temperature-insensitive composite micromechanical resonators," *J. Microelectromechanical Systems*, vol. 18, no. 6, pp. 1409–1419, Dec. 2009.



Siping Wang (S'12) graduated from Cornell University with a B.S degree in applied engineering physics and electrical engineering. At Cornell, he has worked in the groups of Prof. Paul McEuen and Prof. Michel Louge, and in the SRF laboratory at LEPP.

Siping is currently working towards his Master of Science degree in the Department of Electrical Engineering and Computer Science at Massachusetts Institute of Technology in Professor Dana Weinstein's HybridMEMS group. His research interests include gallium nitride (GaN) BAW/SAW resonators and filters, acoustic meta-material for sensing and RF signal processing, computational approaches for device modeling and optimization, wireless sensor networks, and IoT (Internet of Things). Siping is also a Lockheed Martin-MIT Energy Fellow.



Wen-Chien Chen (S'08–M'14) received B.S. degrees in mechanical and mechatronic engineering from National Taiwan Ocean University, Keelung, Taiwan, in 2006, and the M.S. and Ph.D. degrees in power mechanical engineering from National Tsing Hua University, Hsinchu, Taiwan, in 2008 and 2013, respectively. From mid-2012 to mid-2013, he was with Prof. Dana Weinstein at the Massachusetts Institute of Technology, Cambridge, as a Visiting Student. His doctoral research focused on temperature stability, mechan-

ical frequency tuning, and Q improvement of integrated micromechanical resonators using CMOS-MEMS technology for RF or sensors applications. In 2013, he joined Taiwan Semiconductor Manufacturing Company, Hsinchu, Taiwan, where he is currently a MEMS Product Development Principal Engineer.

Dr. Chen received the First Prize at the NTHU College of Engineering Student Paper Competition, and Best Student Paper Award at the 14th Conference on NanoEngineering and Microsystems in Taiwan in 2011. Together with his advisor and junior-mate, he received Best Student Paper Award at the 2011 Joint Conference of the IEEE International Frequency Control Symposium and European Frequency and Time Forum. In 2012, he was a recipient of the Graduate Students Study Abroad Program sponsored by the National Science Council.



Bichoy Bahr (M'12) received his B.Sc. degree with honors in electrical engineering in 2008 and his M.Sc. degree in electrical engineering in 2012, both from Ain Shams University, Cairo, Egypt. He worked as Analog/Mixed Signal and MEMS modeling/design engineer at MEMS Vision, Egypt. Bichoy is currently working towards the Ph.D. degree in the Department of Electrical Engineering at Massachusetts Institute of Technology (MIT). He is affiliated with the HybridMEMS group at MIT. His research interests include the modeling and design of monolithically integrated hybrid CMOS-MEMS unreleased resonators. He is also interested in multi-GHz MEMS oscillator circuits.



Weileun Fang was born in Taipei, Taiwan. He received his Ph.D. degree from Carnegie Mellon University in 1995. His doctoral research focused on determining the mechanical properties of thin films using micromachined structures. In 1995, he worked as a postdoctoral researcher at Synchrotron Radiation Research Center, Taiwan. He joined the Power Mechanical Engineering Department at the National Tsing Hua University (Taiwan) in 1996, where he is now a Distinguished Professor as well as a faculty of the NEMS Institute. In 1999, he was with Prof. Y.-C. Tai at California Inst. Tech. as a visiting associate. His research interests include MEMS with emphasis on micro-fabrication/packaging technologies, CMOS MEMS, CNT MEMS, micro-optical systems, micro-sensors and actuators, and characterization of thin film mechanical properties. Prof. Fang has published more than 140 SCI journal papers, nearly 250 international conference papers, and 80 patents (all in the MEMS field). He is now the Editor-in-Chief of *JMM*, the Board Member of IEEE TDMR, and the Associate Editor of *IEEE Sensors J.*, and *Sensors and Actuators A*. He served as the chief delegate of Taiwan for World Micromachine Summit (MMS) from 2008–2012, and chaired the MMS 2012. He also served as the TPC of IEEE MEMS conference, the EPC of Transducers conference, and the regional co-chair as well as TPC chair of IEEE Sensors conference. He has become the member of international steering committee of Transducers from 2009. Moreover, he also serves as a technical consultant for many MEMS companies in Taiwan.



Sheng-Shian Li (S'04–M'07) received the B.S. and M.S. degrees in mechanical engineering from National Taiwan University in 1996 and 1998, respectively, and the M.S. and Ph.D. degrees from the University of Michigan, Ann Arbor, MI, USA, in 2004 and 2007, respectively, both in electrical engineering and computer science. In 2007, he joined the RF Micro Devices, Greensboro, NC, USA, where he was an R&D Senior Design Engineer until mid-2008 for the development of MEMS resonators and filters. In 2008, he joined the Institute of NanoEngineering and MicroSystems, National Tsing Hua University, Hsinchu, Taiwan, where he is currently an Associate Professor. His research interests focus on nano/microelectromechanical systems, integrated resonators and sensors, RF MEMS, CMOS-MEMS technology, front-end communication architectures, and integrated circuit design and technology. Dr. Li received the Teaching Excellence Award from the College of Engineering, National Tsing Hua University, in 2011. In 2013, Dr. Li also received the Young Faculty Research Award from the National Tsing Hua University and the Ta-Yu Wu Memorial Award from the Ministry of Science and Technology of Taiwan. Together with his students, he received the Best Student Paper Awards at the 2011 IEEE International Frequency Control Symposium and the 2012 IEEE Sensors Conference. He also served as the TPC of the IEEE International Frequency Control Symposium (IFCS) and the IEEE Sensors Conference. He served as the local organizing committee chair for the 2014 IEEE IFCS.



Dana Weinstein is the Finn Associate Professor in the Department of Electrical Engineering and Computer Science at MIT, and a member of the Microsystems Technology Laboratories. Dana received her B.A. in physics from UC-Berkeley in 2004, where she worked on ultra-fast X-ray physics at the Advanced Light Source. She then moved to Cornell University, where she completed her Ph.D. in applied physics in 2009, working on RF Micro Electro-Mechanical Systems (MEMS). The HybridMEMS Lab at MIT led by Prof. Weinstein focuses on development of novel MEMS-enhanced electron devices and systems for high performance, low power consumption, programmable electromechanical signal processors operating in real time at carrier frequencies. Dana is the recipient of the NSF CAREER Award, the DARPA Young Faculty Award, the Intel Early Career Award, and the IEEE IEDM Roger A. Haken Best Paper Award.